AIAA JOURNAL
Vol. 30, No. 8, August 1992

# Joint Computational/Experimental Aerodynamics Research on a Hypersonic Vehicle, Part 1: Experimental Results

William L. Oberkampf* and Daniel P. Aeschliman†
*Sandia National Laboratories, Albuquerque, New Mexico 87185*

**Aerodynamic force and moment measurements and flow visualization results are presented for a hypersonic vehicle configuration at Mach 8. All of the experimental results were obtained in the Sandia National Laboratories Mach 8 hypersonic wind tunnel for laminar boundary-layer conditions. The basic vehicle configuration is a spherically blunted 10-deg half-angle cone with a slice parallel with the axis of the vehicle. On the slice portion of the vehicle, a flap can be attached so that deflection angles of 10, 20, and 30 deg can be obtained. Surface flow visualization showed separated flow in front of each flap configuration. A detailed uncertainty analysis was conducted to estimate the contributors to body force and moment measurement uncertainty. In this paper, comparisons are made with computational results to evaluate both the experimental and numerical results. This extensive set of high-quality experimental force and moment measurements is recommended for use in the calibration and validation of relevant computational aerodynamics codes.**

## Nomenclature

$C_a$ = forebody axial force coefficient, $A/(q_\infty S)$
$C_m$ = pitch moment coefficient, $M/(q_\infty S D_b)$, referenced about $x/L = 0.5$
$C_n$ = normal force coefficient, $N/(q_\infty S)$
$D_b$ = diameter of the base, 4.0 in.
$L$ = body length, 10.391 in.
$M_\infty$ = freestream Mach number
$p_o$ = total pressure
$q_\infty$ = freestream dynamic pressure
$R_L$ = freestream Reynolds number based on body length
$S$ = reference area, 11.525 in.$^2$
$T_o$ = total temperature
$T_w$ = model wall temperature
$x_{cp}$ = axial center of pressure measured from the nose
$\alpha$ = angle of attack, positive when slice on windward side
$\delta$ = flap deflection angle
$\phi$ = model roll angle, 0 deg for slice on windward side at positive $\alpha$

## Introduction

ALTHOUGH in recent years design of flight vehicles has been based increasingly on computational aerodynamics simulation, wind-tunnel experimentation continues to play the major role in aerodynamic analysis and design. This role, however, is changing because of significant improvements in the capability of and confidence in numerical simulations. For a small class of supersonic and hypersonic flow problems, high-quality numerical solutions are now believed to represent the physics of the problem more accurately than a wind-tunnel experiment can simulate the free-flight conditions. An example of this is the supersonic or hypersonic, laminar, perfect gas flow over a simple geometry at low angle of attack.

The realization that certain flowfields can be computed more accurately than they can be measured experimentally must begin to change the relationship between computational and experimental aerodynamics. This paper and its companion paper[1] address this changing relationship and seek to improve the synergism between computational aerodynamics and wind-tunnel experimentation. The purpose of this project is to improve the confidence and accuracy in both wind-tunnel measurements and computational aerodynamic predictions. The physical and numerical approaches can each gain from this joint endeavor by using the strengths of one approach to offset the weaknesses of the other, and vice versa. In this project, experiments and computations were jointly conducted for hypersonic, perfect gas, laminar flow over a hypersonic vehicle geometry. The model geometry was designed so that it could easily be modified to produce a range of flow characteristics. For the simplest configuration, we developed higher confidence in the quality of the computational fluid dynamic (CFD) solutions than the experiment. For the more complex configurations, however, the reverse was true.

In experiments designed to validate CFD codes, experimentalists must develop a better understanding of the assumptions made in the numerical simulation so that experiments can be designed that match these assumptions. For example, in choosing a body geometry with which to validate a CFD code, a configuration should be chosen that eliminates unnecessary numerical difficulties. In the present experiment, this is achieved by requiring the body flap to extend to the base plane of the body for all flap deflections. Although this would be unrealistic in actual flight vehicle hardware, it allows a great simplification in body geometry description and outflow boundary conditions in the numerical simulation.

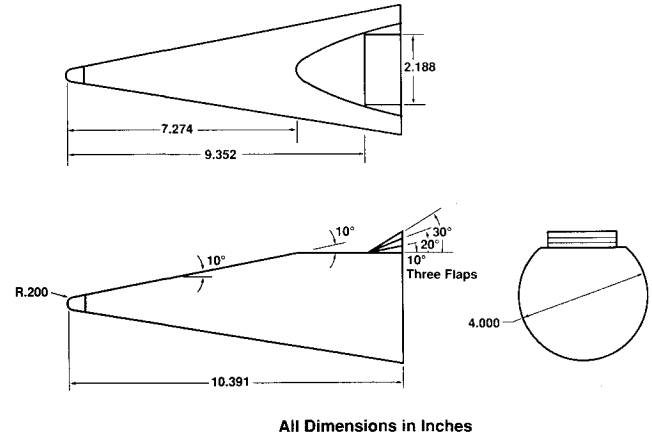


**Fig. 1 Wind-tunnel model.**

Presented as Paper 91-0298 at the AIAA 29th Aerospace Sciences Meeting, Reno, NV, Jan. 7–10, 1991; received March 9, 1991; revision received Jan. 30, 1992; accepted for publication Jan. 30, 1992. 

*Senior Member Technical Staff, Aerodynamics Department, Org. 1554. Associate Fellow AIAA.
†Distinguished Member Technical Staff, Aerodynamics Department, Org. 1554. Member AIAA.

In this paper, aerodynamic force and moment measurements and flow visualization results are presented for a hypersonic vehicle configuration at Mach 8. All of the results were obtained in the Sandia Mach 8 long-duration, blowdown, hypersonic wind tunnel. The basic vehicle configuration is a spherically blunted cone with a slice parallel with the axis of the vehicle. The half-angle of the cone is 10 deg, and the ratio of spherical nose radius to base radius is 10%. Flaps can be attached to the slice portion of the vehicle so that deflection angles of 10, 20, and 30 deg are obtained. Surface flow visualization shows separated flow in front of each flap configuration. An extensive uncertainty analysis was conducted to estimate quantitatively the accuracy of the measurement. The innovative uncertainty analysis was also able to segregate the contributions to uncertainty into two different causes. In this paper, comparisons are made with computational results to evaluate both the experimental and numerical results. More complete computational results for the same geometry and wind-tunnel conditions are given in a companion paper.[1]

## Experimental Apparatus

### Wind Tunnel

The Sandia National Laboratories blowdown-to-vacuum hypersonic wind tunnel consists of three contoured axisymmetric nozzles, arranged like a Gatling gun around a common hub. The test section Mach numbers are nominally 5, 8, and 14. Each nozzle is provided with its own electric resistance heater to prevent flow condensation in the test section. Mach 8 operation uses dry nitrogen, and the total pressure $p_o$ is variable from 250 to 1000 psi. Depending on electrical heating power and nitrogen flow rate, total temperature $T_o$ can be varied from 950 to 1650°R. The available ranges of $p_o$ and $T_o$ provide a unit Reynolds number range of $0.8\text{–}6.2 \times 10^6$/ft. During a run, the total pressure is manually controlled, but all other operating parameters are automatically controlled through a Hewlett-Packard 1000 F-series computer. Slight variations in $p_o$ and $T_o$ occur during a run, approximately 4 and 3%, respectively. Force and moment measurements at each angle of attack, however, are nondimensionalized to the instantaneous $p_o$ and $T_o$ value corresponding to that point. Usable run times are typically 30–60 s, depending on flow Reynolds number, and turnaround time between runs is 1 h or less.

The Mach 8 test section has a diameter of 14 in. and is provided with 8 × 15-in. schlieren-grade windows on the top, bottom, and sides. The windows provide access for a variety of optically based flow diagnostics. Currently, these include surface flow visualization using liquid crystals, schlieren video and photography, and laser holographic interferometry for flow density measurement. Model pitch angle (angle of attack) is varied using a computer-controlled arc-sector drive. Model roll angle and configuration modifications can be changed easily between runs. The entire aft portion of the test section housing retracts rearward to provide easy access to the model.

### Model Geometry

A vehicle geometry was carefully chosen for this project that would allow exploration of the strengths and weaknesses of both numerical and physical experiments. The selected geometry is a 10% spherically blunted cone with a slice on the windward side (see Fig. 1). The geometry has two nose tips, a spherically blunted tip and a sharp conical tip, to provide additional flexibility in altering the boundary-layer transition point on the model. The slice is parallel to the axis and begins at 0.7 of the length of the body, measured from the spherical nose. The model was designed so that three different flaps can be attached to the aft portion of the slice, providing deflection angles of 10, 20, and 30 deg. The trailing edge of each flap extended completely to the base of the body. As noted earlier, this was done to simplify the outflow boundary conditions in the Navier-Stokes codes.

**Table 1 Run number summary**

| $\phi$, deg | $\delta = 0$ deg | $\delta = 10$ deg | $\delta = 20$ deg | $\delta = 30$ deg |
|---|---|---|---|---|
| | Tunnel station 7.6 in. | | | |
| 0 | 34,36,37,73 | 63,72 | 64,71 | 65,70 |
| 90 | 39 | 66,67 | 69 | 68 |
| 180 | 40 | 55 | 56,57 | 58 |
| 270 | 41 | 62 | 61 | 59,60 |
| | Tunnel station 4.1 in. | | | |
| 0 | 74,75 | 83 | 82 | 81 |
| 180 | 76,77 | 78 | 79 | 80 |

### Instrumentation

Forces and moments on the model are derived from a six-component, temperature-compensated strain gauge balance mounted internal to the model. The axial location of the balance was chosen so that the center of pressure normally lay between the balance gauges. A careful calibration of the balance was performed before the start of the experimental program; the resulting matrix of second-order interaction coefficients was then used in all data reduction. Check weights were hung periodically throughout the test series to ensure absence of zero shift or linearity change.

It was essential to determine base pressure accurately because of the relatively large contribution of the base pressure to the axial force coefficient. Base pressure was measured at five locations at varying radial and circumferential positions on a base plate mounted just aft of the model. The base plate was a sharp-edged plate set aft 0.065 in. from, and parallel to, the model base. The circumferential contour of the plate was 0.2 in. radially inward from the edge of the base of the model, and it did not touch the model at any point. The five base pressure orifices were located on the base plate so that the pressure measured was actually the pressure in the gap between the model and the base plate. The local pressure on the base plate was assumed to exist on the adjacent point on the base of the model. This assumption is justified because there would not be a pressure gradient between adjacent points of the flow between parallel plates. The base plate orifice locations were selected to represent equal base areas so that the total axial force on the base of the model was simply the average of all five measurements. The base pressures were measured using Validyne Model AP-10, 0–0.1 psia absolute pressure transducers mounted inside the tunnel to minimize tubing lengths and pressure lag.

To provide thermal boundary conditions on the model surface for the CFD simulations, thermocouples were mounted on the inner surface of the thin-walled (0.1 in.) model. Two thermocouples were mounted in the plane of symmetry on the slice side of the model, and two were mounted 180 deg circumferentially around the model. One pair was located 6 in. from the nose, and the other was 7 in. from the nose. The wall temperature during a run at these locations varied from 535 to 590°R. Because of the very high heat transfer rate near the nose, it is certain that the surface temperature farther forward was higher than temperatures measured with the thermocouples.

Shear-stress-sensitive, temperature-insensitive liquid crystals[2,3] were used in an attempt to help determine the state of the boundary layer (laminar, turbulent, or transitional) and also to visualize surface flow phenomena. Given the proper sensitivity to shear stress, these temperature-insensitive liquid crystals (LCs) change the color of reflected white light as the level of shear stress changes. The color response time to shear stress is approximately a few milliseconds,[3] and the color changes are entirely reversible. Quantitative calibration of the reflected colors in terms of shear stress has not been successful; therefore, the technique is entirely qualitative.

## Experiment Description

### Experimental Conditions

As this experiment was designed to be jointly conducted with a numerical simulation, it was important that the state of the boundary layer was known with confidence. Liquid crystals were applied to the surface of the model to determine whether the boundary layer was laminar or turbulent. A Reynolds number of $1.80 \times 10^6$, based on model length, was chosen so that laminar flow was assured over the length of the vehicle for all angles of attack. The average stagnation conditions were $T_o = 1106°R$ and $p_o = 340$ psia, and freestream Mach number and dynamic pressure were 7.84 and 1.727 psi, respectively.

The angle of attack was varied from $-10$ to 18 deg. The nominal angles of attack at which forces and moments were measured were $-10$, $-7$, $-4$, $-1$, 0, 2, 5, 8, 11, 14, 16, and 18 deg. The roll angle was set at 0 (slice on the windward side), 90, 180, and 270 deg. The primary purpose for the four roll angles was to quantify the effect on aerodynamic forces and moments of any possible flowfield nonuniformities in the wind tunnel. These multiple roll angles were necessary in estimating the uncertainty bounds on the force and moment measurements.

### Experimental Procedure and Data Acquisition

Listed in Table 1 is a complete run schedule for the experiment. As can be seen from the table, several body geometry and roll angles have multiple runs. This was done to aid in the quantitative uncertainty analysis discussed in the next section. In addition, two different axial locations in the test section were used. This was done so that uncertainty due to possible flowfield variations from one tunnel station to another could be evaluated.

Sting deflection at angle of attack and yaw (model rolled 90 deg) was accounted for in all force and moment measurements. The angular corrections for the observed aerodynamic loads were linear with pitch angle and were a maximum of 0.10 deg at the maximum angle of attack.

During preliminary runs, all five base pressures were recorded at a high data rate and subsequently displayed on a strip chart recorder to assess the pressure lags in the system. The pressure stabilization times required were significant, up to 4 s after a continuous 10 deg change in angle of attack. These data were then used to preset the pitch mechanism pause time between $\alpha$ changes to ensure that all base pressures were stable before data acquisition. This pressure stabilization time constraint limited the number of individual angles of attack at which force and moment measurements could be made. (See Ref. 4 for more details.)

### Uncertainty of Measurements

In surveying the literature documenting a wide variety of wind-tunnel experiments, one rarely finds an analysis conducted to quantify the uncertainty of the measurements. Many times this lack is justified because of the press of time or budget constraints. In experiments designed to validate CFD codes, however, this is strongly believed to be unacceptable. In experiments of this type, special attention should be given to constructing the run schedule to maximize information for an uncertainty analysis and then to quantitatively analyze mea-

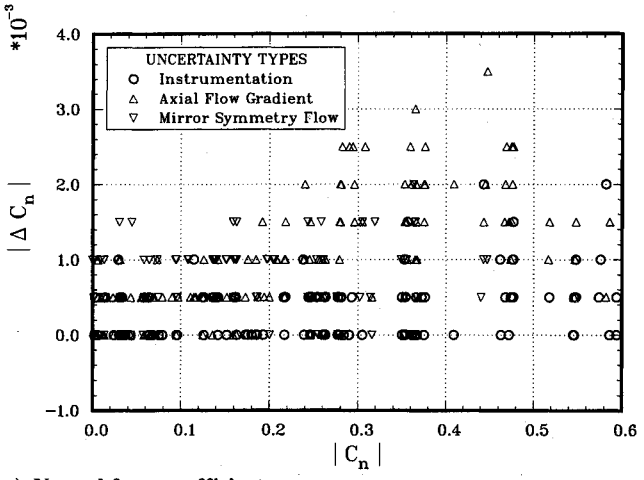


a) Normal force coefficient

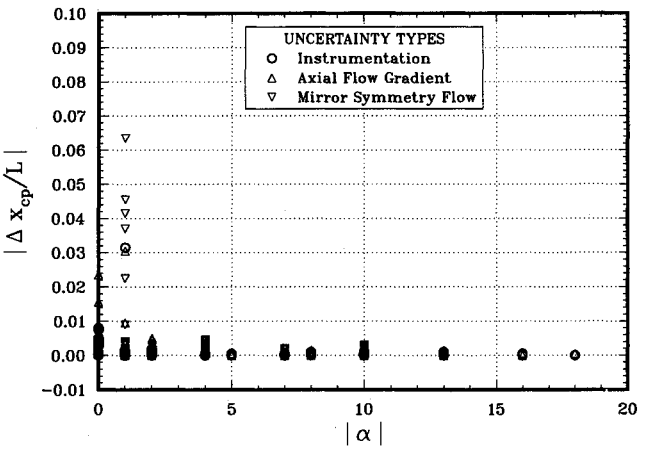


c) Axial center of pressure

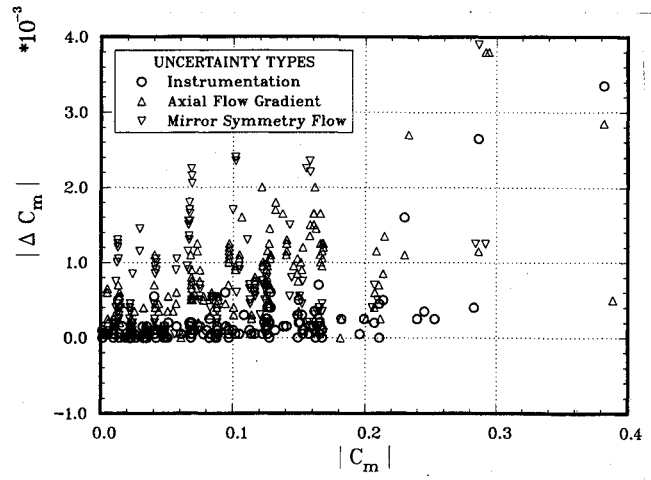


b) Pitch moment coefficient

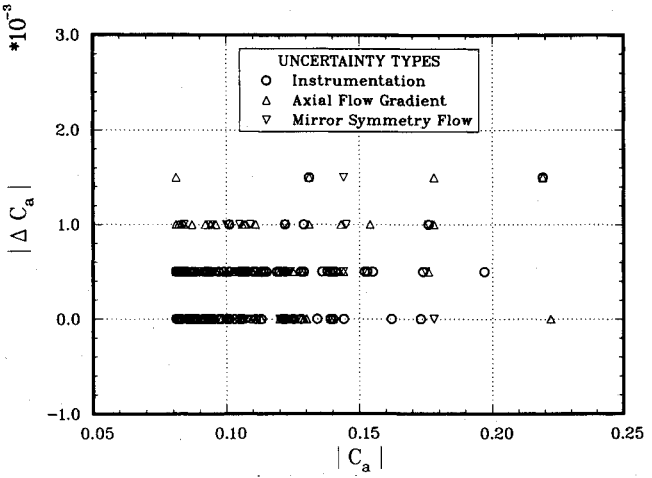


d) Forebody axial force

Fig. 2 Residuals of experimental measurements.

surement uncertainty. Typical uncertainty analyses consider the repeatability of individual instrumentation components such as freestream conditions in the test section, strain gauges, and pressure transducers.[5] It is clear from using this type of procedure that certain factors contributing to measurement uncertainty are not included: for example, uncertainty due to freestream flow nonuniformities and the interaction of various instrumentation components. An innovative procedure was devised in the current effort that is able to quantify the total uncertainty of force and moment measurements. Further, this procedure is able to delineate the uncertainty into two components. This analysis is an experimentally based statistical estimate of variance components of forces and moments. The two uncertainty components are referred to as instrumentation uncertainty and test section flowfield nonuniformity.

The instrumentation uncertainty is that uncertainty in body forces and moments caused by all of the following: strain gauge hysteresis, nonlinearity, thermal sensitivity shift, and thermal zero shift; the analog acquisition reduction system; the data recording system; model pitch, roll, and yaw alignment; run-to-run variations in setting freestream conditions in the test section; and base pressure transducers and instrumentation for eliminating base drag. That is, the instrumentation uncertainty combines all uncertainty components in the entire experiment except those due to test section flowfield nonuniformity. To calculate the instrumentation uncertainty, one compares body force and moment measurements for the same physical location in the test section. By examining the run schedule, Table 1, one can choose run pairs that have the same pitch and roll angles and the same location in the test section and then make comparisons between the measured body force and moment coefficients. Typical run pairs that can be formed are [34,36], [37,73], [56,57], and [74,75]. The total number of run pairs that can be formed for quantifying the instrumentation uncertainty is 14.

Let the difference between an individual force and moment measurement and the average measurement at each angle of attack be defined as the local residual $\Delta$,

$$
\begin{aligned}
(\Delta C_n)_{\alpha_i} &= (C_n)_{\alpha_i} - \overline{(C_n)}_{\alpha_i}, \qquad i = 1,2,\ldots,I \\
(\Delta C_m)_{\alpha_i} &= (C_m)_{\alpha_i} - \overline{(C_m)}_{\alpha_i}, \qquad i = 1,2,\ldots,I \\
(\Delta x_{cp})_{\alpha_i} &= (x_{cp})_{\alpha_i} - \overline{(x_{cp})}_{\alpha_i}, \qquad i = 1,2,\ldots,I \\
(\Delta C_a)_{\alpha_i} &= (C_a)_{\alpha_i} - \overline{(C_a)}_{\alpha_i}, \qquad i = 1,2,\ldots,I
\end{aligned} \tag{1}
$$

where $\overline{\ }$ is the average value for each run pair at each angle of attack, and $I$ is the maximum number of angles of attack that are in common for the run pairs formed. The total number of instrumentation residuals, i.e., measurements at each pitch angle, is 320 for each quantity: normal force, pitch moment, center of pressure, and axial force. (See Ref. 4 for more details.)

The uncertainty in body forces and moments due to a combination of instrumentation uncertainty and test section flowfield nonuniformity can be computed by comparison of certain runs. The uncertainty due solely to test section flowfield nonuniformity, hereafter referred to as flow nonuniformity, can be calculated by statistical methods. This will be discussed later. Combined instrumentation and flow nonuniformity un-

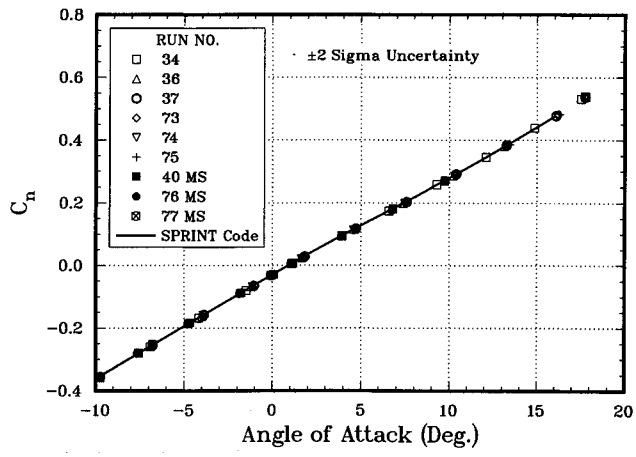


a) Normal force coefficient

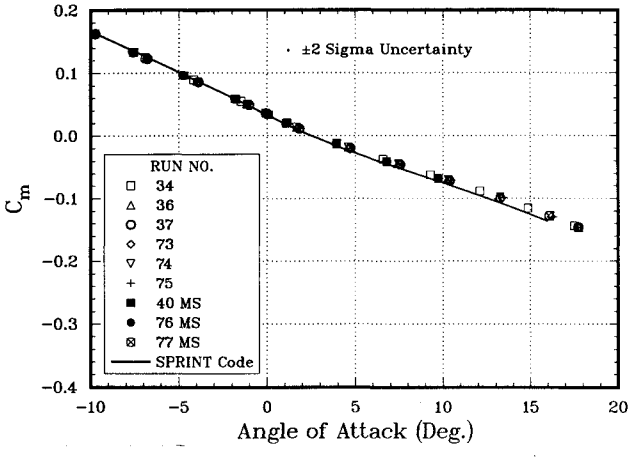


b) Pitch moment coefficient

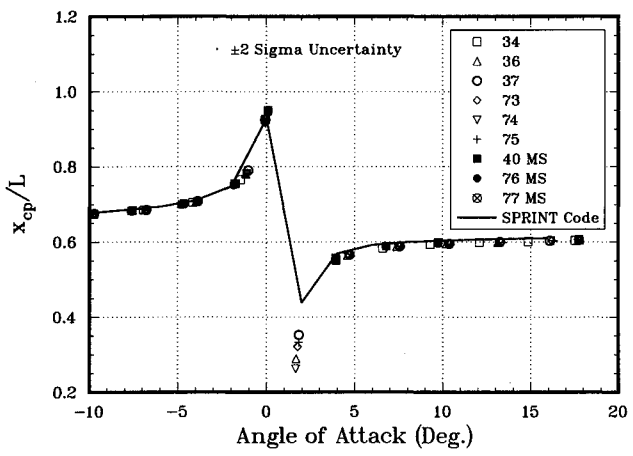


c) Axial center of pressure

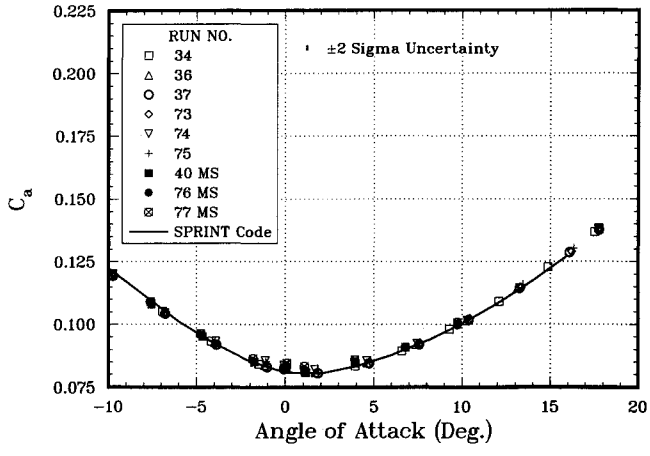


d) Forebody axial force coefficient

**Fig. 3 Force and moment coefficients for slice-only configuration.**

**Table 2 Summary of results for uncertainty analysis**

| Uncertainty Type | $C_n$ | | $C_m$ | | $x_{cp}/L$ | | $C_a$ | |
|---|---|---|---|---|---|---|---|---|
| | $\hat{\sigma}$ | % | $\hat{\sigma}$ | % | $\hat{\sigma}$ | % | $\hat{\sigma}$ | % |
| Instrument | $0.474 \times 10^{-3}$ | 20 | $0.406 \times 10^{-3}$ | 19 | $0.413 \times 10^{-3}$ | 9 | $0.426 \times 10^{-3}$ | 63 |
| Flow | $0.941 \times 10^{-3}$ | 80 | $0.851 \times 10^{-3}$ | 81 | $1.322 \times 10^{-3}$ | 91 | $0.324 \times 10^{-3}$ | 37 |
| Total | $1.054 \times 10^{-3}$ | 100 | $0.943 \times 10^{-3}$ | 100 | $1.385 \times 10^{-3}$ | 100 | $0.535 \times 10^{-3}$ | 100 |

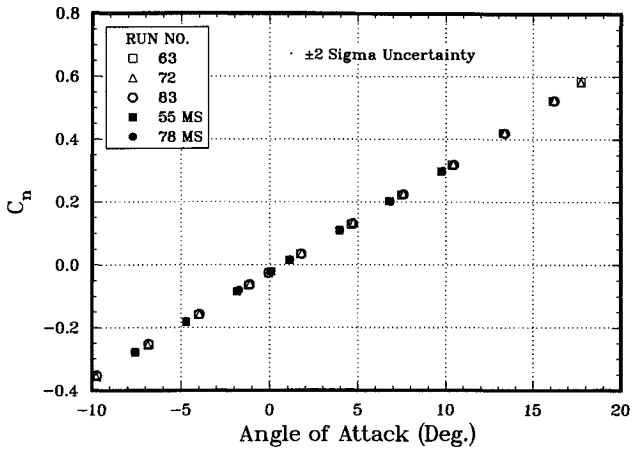


a) Normal force coefficient

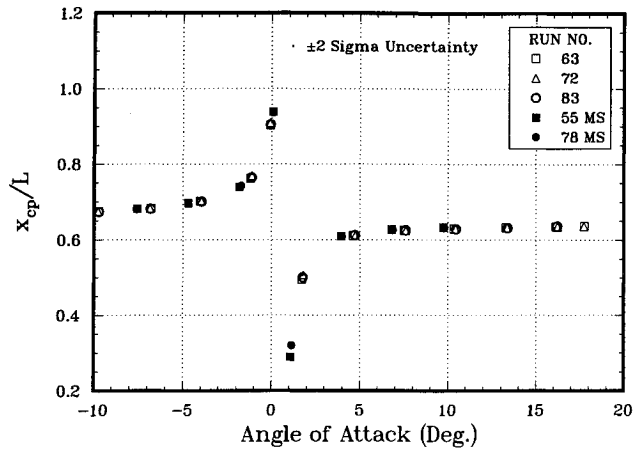


c) Axial center of pressure

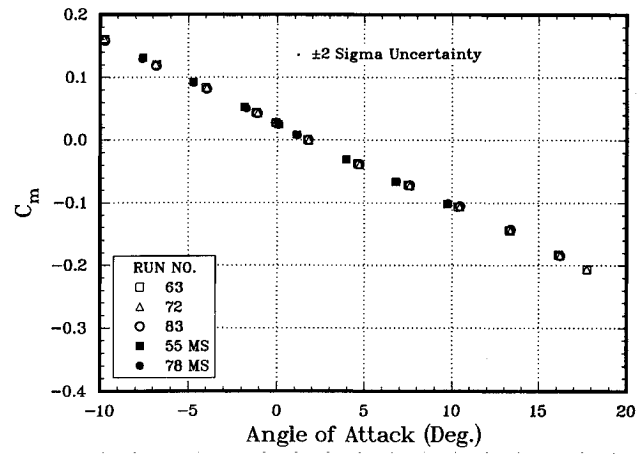


b) Pitch moment coefficient

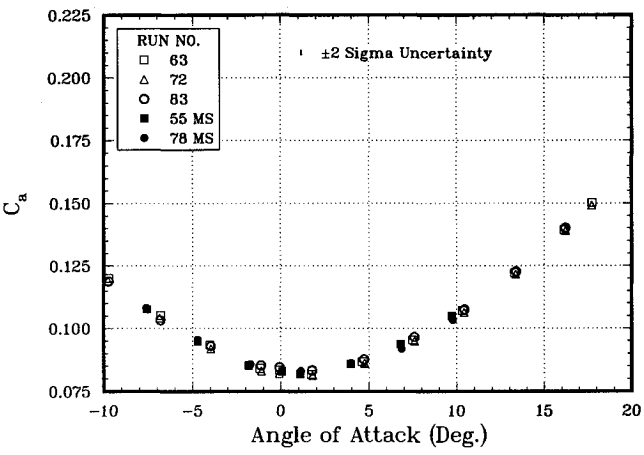


d) Forebody axial force coefficient

**Fig. 4 Force and moment coefficients for 10-deg flap configuration.**

certainty are calculated by comparing force and moment measurements when the model is at physically different locations in the test section. By examining the run schedule, Table 1, one finds two different ways of attaining different locations in the test section. The first method forms run pairs that have the same roll angle and flap angle, but are at different axial stations in the test section. Typical run pairs that can be formed are [34,74], [37,75], [64,82], and [58,80]. The total number of run pairs that can be formed in this way is 20.

The second method forms run pairs based on mirror symmetry between the model at a roll angle of 0 deg and pitched to a positive angle of attack, and the model at a roll angle of 180 deg and pitched to the same negative angle of attack. The mirror symmetry pairs are formed for both runs at the same axial station. As the maximum negative angle of attack was $-10$ deg, the residuals for individual angles of attack can only be calculated over the range $-10$ to $+10$ deg. Typical run pairs that can be formed are [34,40], [64,56], [74,76], and [81,80]. The total number of run pairs that can be formed in this way is 19. The total number of residuals, from both types of run pairs, that combine instrumentation and flow nonuniformity is 740 for each quantity: normal force, pitch moment, center of pressure, and axial force.

Figure 2 shows the magnitude of the residuals vs the magnitude of the quantity measured, except for center of pressure, which is plotted vs magnitude of angle of attack. These plots include all of the residuals for both instrumentation and flow nonuniformity components. The residuals are plotted vs magnitude of the measurement because normally the magnitude of the uncertainty increases as the magnitude of the quantity measured increases. For example, instrument uncertainty typically is quoted as a constant value plus percent of reading. These plots minimally show this trend. The "quantized" character of $\Delta C_n$ and $\Delta C_a$, Figs. 2a and 2d, is due to the limit of resolution of the digitized signal from the strain gauge balance.

In Fig. 2, "axial gradient flow" refers to residuals calculated from flow nonuniformity run pairs at different tunnel axial stations, and "mirror symmetry flow" refers to run pairs formed from angle-of-attack mirror symmetry at each axial station. It can be seen qualitatively in Fig. 2 that the residuals for $C_n$, $C_m$, and $C_a$ are dominated by flow nonuniformity, not instrumentation uncertainty. The contributions from axial

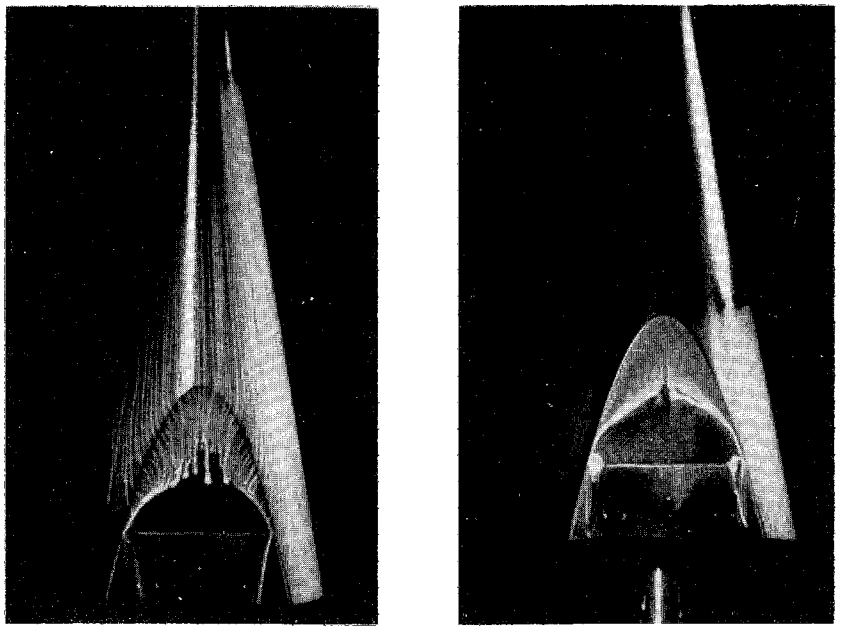

a) $\alpha = 0$ deg b) $\alpha = 10$ deg

**Fig. 5 Surface flow visualization for 10-deg flap deflection.**

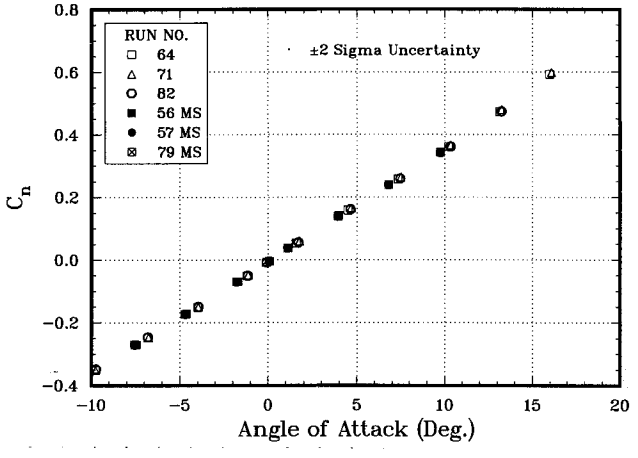


a) Normal force coefficient

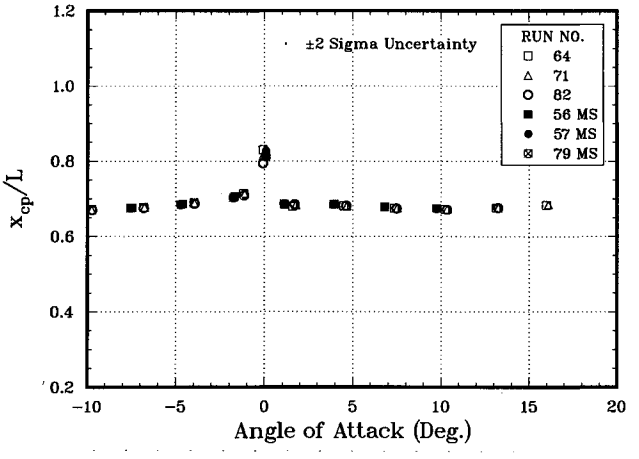


c) Axial center of pressure

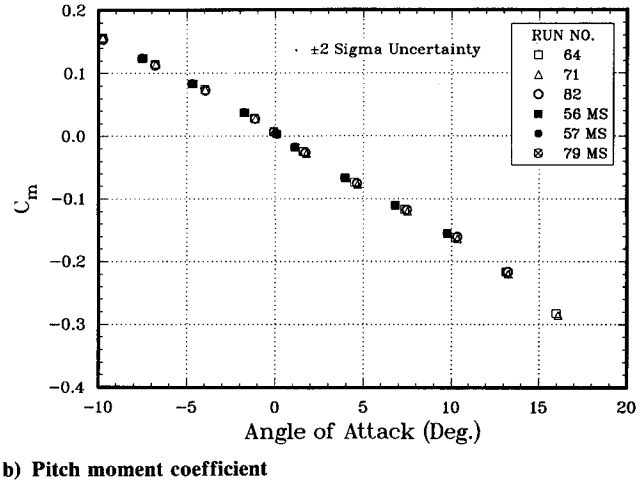


b) Pitch moment coefficient

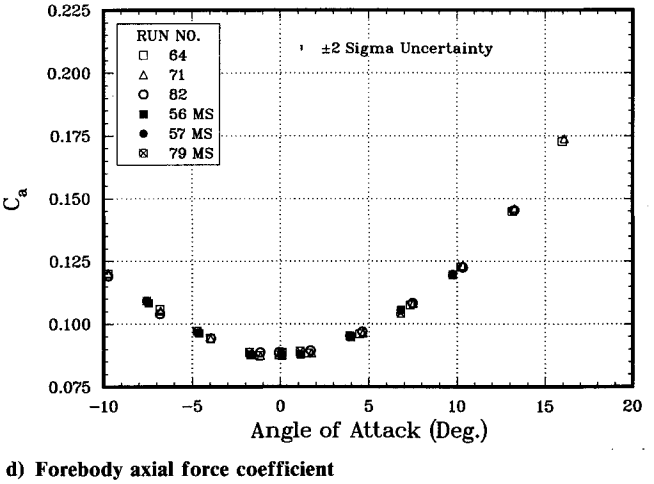


d) Forebody axial force coefficient

**Fig. 6 Force and moment coefficients for 20-deg flap configuration.**

flow gradient and cross-tunnel flow gradient (mirror symmetry flow) are equally contributing to the uncertainty. (In Ref. 6, it was concluded from the uncertainty analysis that the primary contributor to the total uncertainty was due to nonreflective symmetry of the freestream flow. Further investigation into this matter showed that this anomaly was due to a data reduction error, which has since been corrected. See Ref. 4 for details.) The residuals for $x_{cp}/L$, Fig. 2c, show the expected trend of increasing uncertainty as the angle of attack approaches zero, more precisely, as the ratio $C_m/C_n$ approaches zero.

The sample variance for the instrumentation component and also for the total experiment (combined instrumentation and flow nonuniformity components) is calculated from the equation

$$\hat{\sigma}^2 = \frac{1}{n}\sum_{j=1}^{n}[\Delta_1^2 + \Delta_2^2]_j$$

where $n$ is the number of local residuals, and $\Delta_1$ and $\Delta_2$ are the residuals for each run pair from Eqs. (1). (Note that estimates, or sample values, are indicated by a caret over the parameter being estimated.) This equation is applied to each quantity: $C_n$, $C_m$, $x_{cp}/L$, and $C_a$. These sample variances are estimates of corresponding instrumentation and combined population variances. The relationship among the population variances is

$$\sigma^2_{\text{combined}} = \sigma^2_{\text{instrumentation}} + \sigma^2_{\text{flow}}$$

because of the independence of instrumentation errors and flow nonuniformities. Thus, given the sample variance due to instrumentation and that for the total experiment, i.e., the combination of the instrumentation and flow, the component due to flow nonuniformity can be estimated by

$$\hat{\sigma}^2_{\text{flow}} = \hat{\sigma}^2_{\text{combined}} - \hat{\sigma}^2_{\text{instrumentation}}$$

Table 2 gives the estimated standard deviation $\hat{\sigma}$ (square root of the variance estimate) due to instrumentation, flow nonuniformity, and the total for each quantity measured in the experiment. Also shown in the table is the percent contribution due to each of the components identified. In the calculation for the standard deviation for $x_{cp}/L$, all residuals for angles of attack of $-1$, 0, and $+1$ deg were excluded. This was done because it is well known that the uncertainty in $x_{cp}$ becomes indefinite as the normal force and pitch moment approach zero. From Table 2 it can be seen that the uncertainty in $C_n$, $C_m$, and $x_{cp}$ due to the entire wind tunnel system instrumentation ranges from 9 to 20%, whereas that due to flow nonuniformity is 80–91%. Although this type of uncertainty analysis is new to wind-tunnel data analysis, it is suspected that most wind tunnel experiments are dominated by flowfield uncertainty and not instrumentation uncertainty. Table 2 shows that the uncertainty in forebody axial force coefficient is 63% due to instrumentation and 37% due to flow. This reversal of uncertainty contributions compared to the other quantities is believed due to instrumentation inaccuracies in removing base drag from the total axial force.

The total uncertainty bound on each measurement with probability, or confidence, 95% is $2\hat{\sigma}$. Therefore, for each measurement, one has $C_n \pm 2\hat{\sigma}$, $C_m \pm 2\hat{\sigma}$, $x_{cp}/L \pm 2\hat{\sigma}$, and $C_a \pm 2\hat{\sigma}$. These uncertainty intervals are of the form: measure-

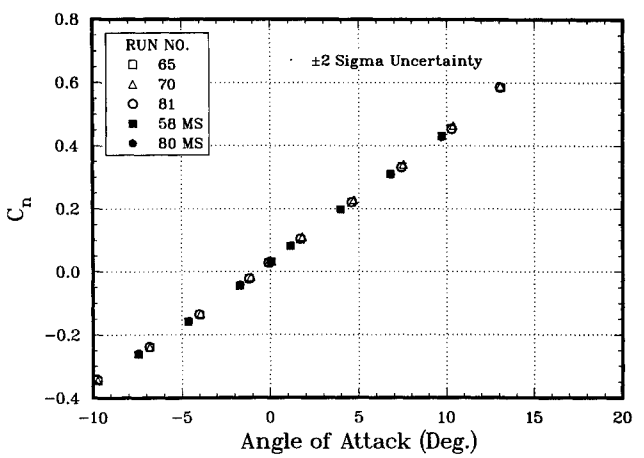


a) Normal force coefficient

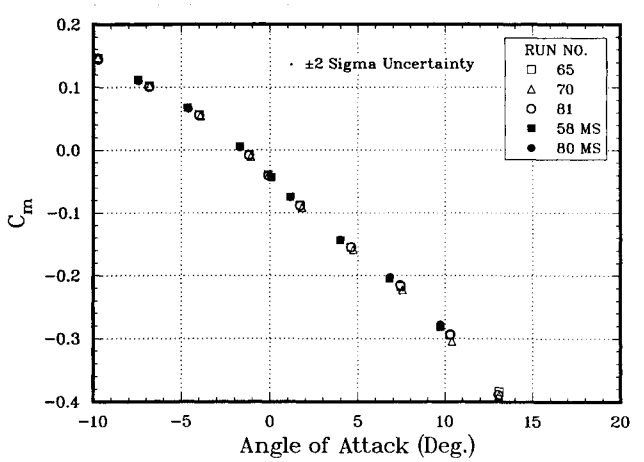


b) Pitch moment coefficient

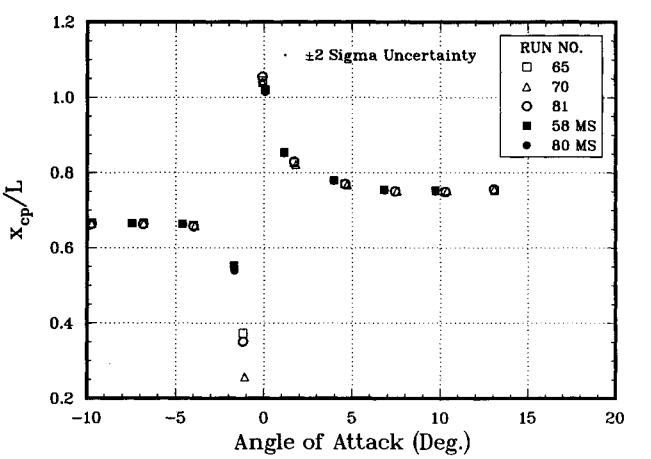


c) Axial center of pressure

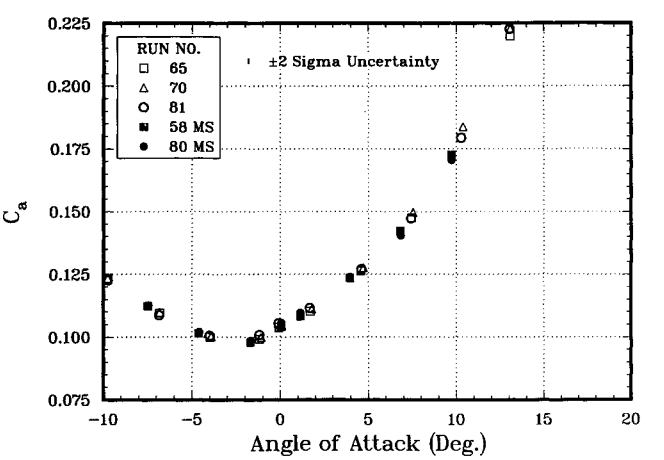


d) Forebody axial force coefficient

Fig. 7 Force and moment coefficients for 30-deg flap configuration.

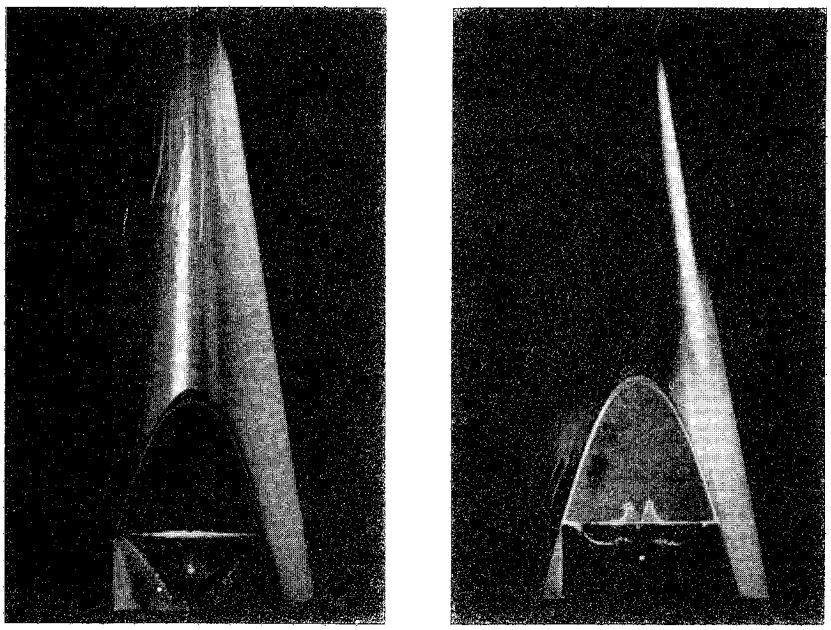

a) $\alpha = 0$ deg b) $\alpha = 10$ deg

**Fig. 8 Surface flow visualization for 20-deg flap deflection.**

ment value plus and minus absolute uncertainty bound, with confidence that 95% of all measurements fall within this bound.

It is firmly believed that this type of uncertainty analysis should be more commonly done by wind-tunnel experimenters so that quantitative uncertainty can be known and, more important, the major contributors to uncertainty can be identified so that the quality of experimental results can be continually improved.

## Results and Discussion

### Laminar Flow Determination

As this experiment was designed to be a CFD validation experiment for laminar flow, it was crucial to choose the proper Reynolds number. It was hoped that the liquid crystal color change diagnostic technique would provide this information, but a satisfactory color change due to shear stress alone was not achieved. The two most sensitive liquid crystals available were used, but they did not produce the color range desired because of the low surface shear stress at the test conditions. They were, however, still very useful in determining laminar and turbulent flow because of their surface flow visualization capability.

Initial boundary-layer determination runs were made with a freestream Reynolds number (based on model length) of $5.0 \times 10^6$. Boundary-layer studies were made at both 0- and 15-deg angle of attack, as it is known that transition can be triggered by crossflow.[7] At this Reynolds number, the surface flow pattern of the liquid crystals showed a distinct surface flow wave pattern at $\alpha = 15$ deg. These waves were first distinguishable at about $x/L = 0.45$ and extended to the base of the model. They were standing waves at an angle of roughly 35 deg to the local surface shear stress. These waves have been observed previously by McDevitt and Mellenthin[8] and Adams[9] in transition studies on hypersonic cones. They are actually stationary vortices near the model surface that occur during the initial instability of the boundary layer before transition. This inflectional instability has been analyzed by Tobak[10] and others. At a Reynolds number of $3.5 \times 10^6$, these waves again appeared, but they began at $x/L = 0.6$ and continued to the base of the body. To attain fully laminar flow, even at the highest angle of attack, the Reynolds number was again reduced, this time to $1.8 \times 10^6$. At this condition, these stationary vortices could be only faintly seen near the base of the body at $\alpha = 15$ deg. Therefore, this Reynolds number was used for all force and moment measurements.

### Slice-Only Configuration

As discussed earlier, the slice-only configuration represents a sufficiently simple geometry, with a laminar boundary layer and only attached flow at low angle of attack. This allows the CFD solution to be computed more accurately than the complete wind-tunnel instrumentation system can measure the forces and moments. Therefore, this case actually represents a validation of the physical experiment. In the companion paper,[1] a detailed grid convergence study was conducted to demonstrate quantitatively the uncertainty of the numerical simulation. For the slice-only configuration, the numerical simulations were shown to contain an absolute error of less than 1% for all force and moment quantities for this configuration.

Figure 3 shows the comparisons between the experimental and numerical results for the slice-only configuration. Figure 3, and every figure showing force and moment measurements, shows data from every run having the same model configuration (see Table 1). That is, plotted in each figure are data from runs that have the same configuration, but at both tunnel axial stations and at a roll angle of 180 deg. The $\phi = 180$ deg are referred to as mirror symmetry (MS) runs in the figures. For example, runs 40, 76, and 77 in Fig. 3 are plotted with the $\phi = 0$ runs by setting $\alpha = -\alpha$, $C_n = -C_n$, and $C_m = -C_m$. The solid lines in the figures are parabolized Navier-Stokes (PNS) calculations using the Sandia code SPRINT. Figure 3a shows excellent agreement between computations and experiment for the normal force coefficient.

Figures 3b and 3c show computations and experiment for the pitch moment coefficient and center of pressure, respectively. It is noted from Fig. 3b that the PNS solution is in excellent agreement with the measurements for low angle of attack, but at large angle of attack, the computations are up to 8% larger (negatively) than the measurements. This disagreement could be due to either slight flow nonuniformities across the test section or inaccuracies in the computations for separated flow on the leeside of the body. Although the wind tunnel test section has been calibrated, the measured test section flow has not been incorporated into the numerical simulation. (See Ref. 4 for more detailed analyses of the differences

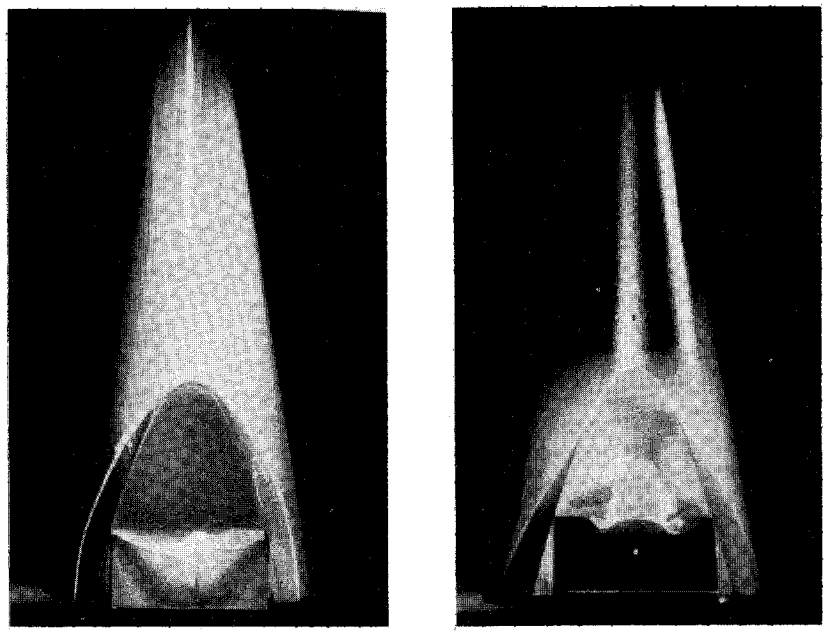

a) $\alpha = 0$ deg b) $\alpha = 10$ deg

**Fig. 9 Surface flow visualization for 30-deg flap deflection.**

between computational and experimental results for the slice-only geometry.)

Figure 3d shows computational and experimental results for the forebody ($p_{base} = p_\infty$) axial force coefficient. Theory and experiment are in very good agreement over the entire angle-of-attack range. Note that the $\pm 2\sigma$ uncertainty bound calculated from the uncertainty analysis is larger for $C_a$ than for the other aerodynamic parameters. This is believed to be primarily due to uncertainty in measuring base pressure. In preliminary experimental work, not allowing all of the base pressure readings to stabilize during the pitch sweep was found to be the dominant contributor to axial force measurement uncertainty. The model pitch timing sequence was then adjusted to minimize this source of error. For hypersonic wind tunnels that use a continuous pitch sweep technique or have very short run times, base pressure stabilization through any tubing length may not be possible. This may require miniature, fast response, surface mounted, base pressure transducers with very high sensitivity for operation at the near vacuum conditions existing in the base flow. Such transducers are not routinely available.

#### 10-Degree Flap Deflection

Figure 4 shows the experimental measurements for the 10-deg flap deflection configuration. (Computational results are not shown for any of the flap deflections because confidence in the accuracy of the solutions diminished for the complex flowfield associated with the flap. See Ref. 1 for comparisons.) All of the aerodynamic forces and moments for the 10-deg flap deflection are similar to the measurements for the slice-only configuration. It is seen that the high pressure on the flap moves the center of pressure slightly aft, as expected. Comparing Fig. 3c with Fig. 4c, one finds that the center of pressure moves aft $0.05L$ for low angle of attack and $0.03L$ for large angle of attack.

Figure 5 shows photographs of the liquid crystals used for surface flow visualization on the 10-deg flap configuration. For $\alpha = 0$, Fig. 5a, the surface flow clearly shows an axially separated region ahead of the flap. The separated region on the slice portion of the body takes on an elliptical shape with the most forward extent occurring on the plane of symmetry. This separated flow region was not expected for the flap deflection of only 10 deg. Its occurrence must be due to the presence of the laminar boundary layer in addition to the relatively large span flap which allows little three-dimensional pressure relief off the sides of the flap. The darker shaded region on the flap is the reattachment region of the separation bubble. Aft of this region, the surface streak lines move toward the base.

Figure 5b shows the windward side surface flow for an angle of attack of 10 deg. The separated region ahead of the flap is somewhat larger than that at $\alpha = 0$. From measurements on the photographs, the axial locations of the beginning of the separated flow regions are $0.83L$ and $0.81L$ for $\alpha = 0$ and 10 deg, respectively. Recall that the slice starts at $0.7L$ and the flap begins at $0.9L$. It should be noted that determination of the size of separated flow regions from surface flow visualization is only approximate because of the finite thickness of the film and the possibly unsteady nature of the flow.

#### 20- and 30-Degree Flap Deflections

Figures 6 and 7 show the experimental measurements for the 20- and 30-deg flap deflections, respectively. For these large flap deflections, it is seen that the center of pressure variation with angle of attack reverses from that seen at low flap angle. Figure 6c shows that the center of pressure for $\delta = 20$ deg is almost constant with both positive and negative angle of attack. For $\delta = 30$ deg, Fig. 7c, $x_{cp}$ moves dramatically forward as the angle of attack increases. This is the opposite trend from the slice-only and 10-deg flap configurations. The computational results for forces and moments on the 20- and 30-deg flap deflections, presented in Ref. 1, show significant differences from the experimental measurements. Although various techniques were tried to improve the predictions, it appears that these large flap deflections generate flowfields that are more difficult to calculate than previously thought.

Shown in Figs. 8 and 9 are the surface flow visualization photographs for the 20- and 30-deg flap deflections. For $\delta = 20$ deg, the separated flow region moves forward almost to the start of the slice. From the photographs, the start of the axially separated flow was measured as $0.72L$ and $0.71L$ for $\alpha = 0$ and 10 deg, respectively. For $\delta = 30$ deg, the separated flow not only moves forward to the start of the slice, but it also spills off the slice and onto the conical portion of the body. From these photographs and also video taken during the runs, it is not clear if the separated flow reattaches onto

the top edge of the flap. There is reason to believe, however, that the flow does not reattach and that reverse flow from the base region is flowing across the flap. If this is proven to be the case, it would represent a serious complication to computational simulations because it may require that the base flow also be calculated as part of the forebody solution.

To assist in the validation of CFD codes, this complete set of aerodynamic force and moment data can be obtained in magnetic media form from the authors upon request.

## Conclusions and Recommendations

Very good agreement between experimental and computational results were obtained for the slice-only model geometry for all force and moment coefficients. For the flap deflection cases, computational results increasingly differed from experimental measurements as the flap deflection increased (see the companion paper[1]). Future plans for this joint computational/experimental program include finely-spaced measurements of the Mach number, dynamic pressure, and flow angularity in the test section of the wind tunnel. The actual nonuniform flowfield of the wind tunnel could then be used in the CFD computations as nonuniform shock boundary conditions. It is strongly believed that this type of synergism between experimental and numerical simulations must take place in the future.

Experimental investigators should take a more constructively critical view toward their measurements, particularly for CFD validation experiments. They should identify and quantify components of uncertainty through detailed uncertainty analyses. Likewise, numerical simulations should routinely include error analyses. With the strengths and weaknesses of each approach openly discussed, a more beneficial and productive relationship can be developed in the future.

## Acknowledgments

This work was performed at Sandia National Laboratories, Albuquerque, New Mexico, and was supported by the U. S. Department of Energy under Contract DE-AC04-76DP00789. The authors thank Roger Tate, Robert Croll, John Henfling, Kenneth Harmon, and Buddy Lafferty of the Aerodynamics Department for their generous and enthusiastic assistance in conducting this experiment. In addition, the data analysis help of Don Larson and Mary Walker of the Computational Fluid Dynamics Department is greatly appreciated. All are staff members at Sandia National Laboratories.

## References

[1]Walker, M. A., and Oberkampf, W. L., "Joint Computational/Experimental Aerodynamics Research on a Hypersonic Vehicle, Part 2: Computational Results," *AIAA Journal,* Vol. 30, No. 8, 1992, pp. 2010–2016.

[2]Reda, D. C., "Observations of Dynamic Stall Phenomena on an Oscillating Airfoil with Shear-Stress-Sensitive Liquid Crystal Coatings," *Proceedings of the 17th International Council of the Aeronautical Sciences,* Stockholm, Sweden, Sept. 1990.

[3]Reda, D. C., and Aeschliman, D. P., "Liquid Crystal Coatings for Surface Shear Stress Visualization in Hypersonic Flows," *Journal of Spacecraft and Rockets,* Vol. 29, No. 2, 1992, pp. 155–158.

[4]Oberkampf, W. L., Aeschliman, D. P., and Tate, R. E., "Experimental Aerodynamics Research on a Hypersonic Vehicle," Sandia National Labs., SAND 92-1411, Sept. 1992.

[5]"Aerodynamic Data Accuracy and Quality: Requirements and Capabilities in Wind Tunnel Testing," AGARD CP-429, Sept. 1987.

[6]Oberkampf, W. L., and Aeschliman, D. P., "Joint Computational/Experimental Aerodynamics Research on a Hypersonic Vehicle: Part 1, Experimental Results," AIAA Paper 91-0298, Jan. 1991.

[7]Balachandar, S., Streett, C. L., and Malik, M. R., "Secondary Instability in Rotating Disk Flow," AIAA Paper 90-1527, June 1990.

[8]McDevitt, J. B., and Mellenthin, J. A., "Upwash Patterns on Ablating and Nonablating Cones at Hypersonic Speeds," NASA TN D-5346, July 1969.

[9]Adams, J. C., Jr., "Three-Dimensional Laminar Boundary Layer Analysis of Upwash Patterns and Entrained Vortex Formation on Sharp Cones at Angle of Attack," Arnold Engineering Development Center, AEDC-TR-71-215, Dec. 1971.

[10]Tobak, M., "On Local Inflexional Instability in Boundary-Layer Flows," *Zeitschrift fur angewandte Mathematik und Physik,* Vol. 24, 1973, pp. 330–354.